NOTE

Magnetic Resonance in Medicine 00:00–00 (2017)

Fast and Reproducible In Vivo T_1 Mapping of the Human Cervical Spinal Cord

Marco Battiston,[1]* Torben Schneider,[2] Ferran Prados,[1,3] Francesco Grussu,[1] Marios C. Yiannakas,[1] Sebastien Ourselin,[3] Claudia A. M. Gandini Wheeler-Kingshott,[1,4,5] and Rebecca S. Samson[1]

Purpose: To develop a fast and robust method for measuring T_1 in the whole cervical spinal cord in vivo, and to assess its reproducibility.

Methods: A spatially nonselective adiabatic inversion pulse is combined with zonally oblique-magnified multislice echo-planar imaging to produce a reduced field-of-view inversion-recovery echo-planar imaging protocol. Multi- inversion time data are obtained by cycling slice order throughout sequence repetitions. Measurement of T_1 is performed using 12 inversion times for a total protocol duration of 7 min. Reproducibility of regional T_1 estimates is assessed in a scan-rescan experiment on five heathy subjects.

Results: Regional mean (standard deviation) T_1 was: 1108.5 ($\pm$77.2) ms for left lateral column, 1110.1 ($\pm$83.2) ms for right lateral column, 1150.4 ($\pm$102.6) ms for dorsal column, and 1136.4 ($\pm$90.8) ms for gray matter. Regional T_1 estimates showed good correlation between sessions (Pearson correlation coefficient = 0.89 (P value $<$ 0.01); mean difference = 2 ms, 95% confidence interval $\pm$ 20 ms); and high reproducibility (intersession coefficient of variation approximately 1% in all the regions considered, intraclass correlation coefficient = 0.88 (P value $<$ 0.01, confidence interval 0.71–0.95)).

Conclusions: T_1 estimates in the cervical spinal cord are reproducible using inversion-recovery zonally oblique-magnified multislice echo-planar imaging. The short acquisition time and large coverage of this method paves the way for accurate T_1 mapping for various spinal cord pathologies. **Magn Reson Med 000:000–000, 2017.**

Key words: spinal cord; reduced FOV; T_1 mapping; reproducibility; inversion Recovery

INTRODUCTION

The longitudinal relaxation time T_1 is one of the most fundamental quantitative parameters in MRI. Several studies have investigated the biological correlates of T_1. It is well-established that T_1 is dependent on myelin content (1). Relaxation of myelin water occurs faster than nonmyelin water; therefore, tissues with higher myelin content show a lower average T_1. However, T_1 has been shown to depend also on additional microstructural features with a constant total myelin volume, such as water content (2), axonal size in white matter (3), and iron concentration in gray matter (4).

Despite the lack of specificity to a single particular biological feature, T_1 is sensitive to changes in tissue microstructure caused by pathologies and inflammatory events. It also provides a quantitative measure comparable across subjects and centers, which is more informative than visual examination of conventional T_1-weighted images. Precise and robust characterization of T_1 in vivo is therefore of great importance. Moreover, the accurate knowledge of T_1 serves as the basis for other quantitative MR methods (e.g., perfusion and quantitative magnetization transfer imaging) and in the optimization of imaging sequence parameters.

Several techniques are available to estimate T_1 in vivo, especially in the brain. Considerable progress has been made in the development of fast mapping techniques: methods such as the Look-Locker inversion recovery (IR) (5,6) and the variable flip angle (VFA) (7,8) are particularly appealing for their ability to achieve T_1 estimates with large coverage in a few minutes of scan time.

[1]NMR Research Unit, Queen Square MS Center, Department of Neuroinflammation, UCL Institute of Neurology, University College London, London, United Kingdom.

[2]Philips Healthcare, Guilford, Surrey, United Kingdom.

[3]Translational Imaging Group, Center for Medical Image Computing, Department of Medical Physics and Biomedical Engineering, University College London, London, United Kingdom.

[4]Department of Brain and Behavioral Sciences, University of Pavia, Pavia, Italy.

[5]Brain MRI 3T Mondino Research Center, C. Mondino National Neurological Institute, Pavia, Italy.

We thank the UK MS Society and the UCL-UCLH Biomedical Research Centre for their ongoing support of the Queen Square MS Centre, and for funding M.B., M.C.Y., and R.S.S. Additionally, we thank the following for grant support: Horizon2020-EU3.1 CDS-QUAMRI (ref. 634541) (F.G.); the Guarantors of Brain Project (F.P.); grants EPSRC EP/I027084/1 and ISRT IMG006; MRC (MR/J500422/1); NIHR BRC UCLH/UCL High Impact Initiative-BW.mn.BRC10269; grants EPSRC (EP/H046410/1, EP/J020990/1, EP/K005278) and MRC (MR/J01107X/1); and the INSPIRED study supported by Wings for Life, Spinal Research and Craig H. Neilsen Foundation (R.S.S.).

Torben Schneider is an employee of Philips Healthcare.

*Correspondence to: Marco Battiston, M.Sc., [1]NMR Research Unit, Queen Square MS Center, Department of Neuroinflammation, UCL Institute of Neurology, University College London, Russell Square House, 10-12 Russell Square, London WC1B 5EH, United Kingdom.
E-mail: marco.battiston.13@ucl.ac.uk; Twitter: @buiceo

Received 17 March 2017; revised 4 July 2017; accepted 5 July 2017

DOI 10.1002/mrm.26852
Published online 00 Month 2017 in Wiley Online Library (wileyonlinelibrary.com).

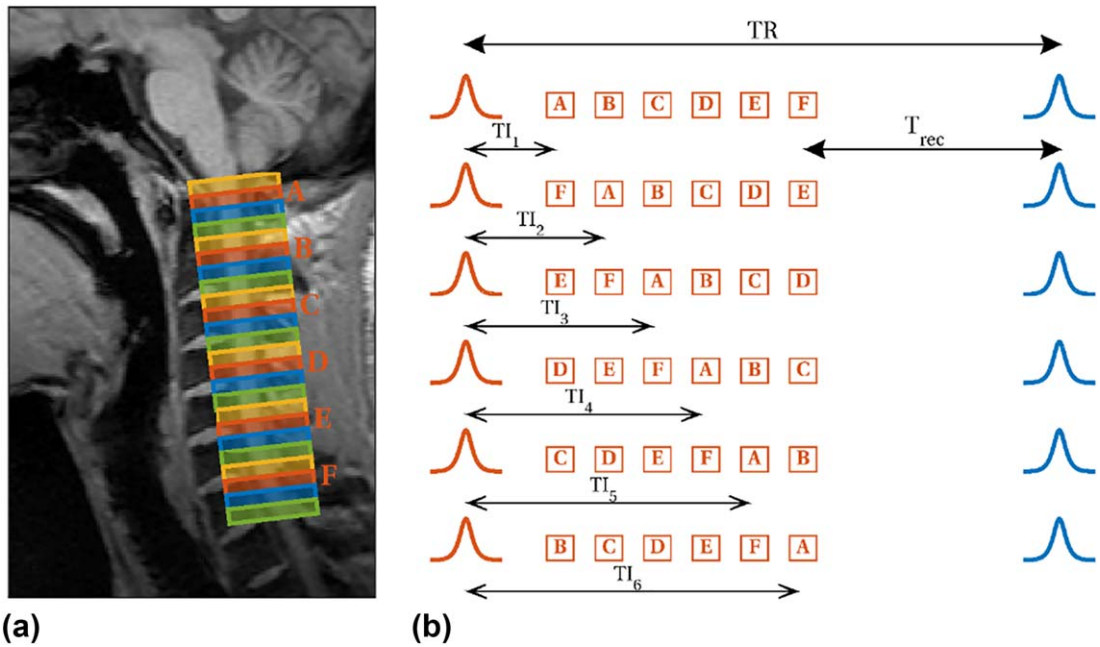

FIG. 1. **a**: Schematic of ZOOM-EPI multislice acquisition in the whole cervical cord, from levels C1 to C7. Slices are grouped in packages (identified by colors); a package is acquired per each TR. Inversion-recovery ZOOM-EPI is implemented by adding a global inversion pulse before each package acquisition (i.e., in each TR). **b**: Between acquisitions of different packages, a recovery time ($T_{rec} > 5$ s) is added to ensure full recovery of magnetization. Slice order is shuffled within packages to avoid TR lengthening in a multi-TI experiment, producing a number of effective TIs equal to the number of slices per package (N_{spp}).

However, great variability among T_1 estimates can be found in literature, which has been ascribed to the sensitivity of the various methods used to site-specific factors such as radiofrequency (RF) field uniformity, RF pulse imperfections, and incomplete spoiling (9). Thus, the time-consuming IR T_1 mapping approach is still regarded as the reference ("gold standard") method for in vivo T_1 measurements.

Development of quantitative MRI techniques for the spinal cord, including the characterization of T_1, generally lags behind the brain (10,11), despite the crucial involvement of the spinal cord in several diseases, such as multiple sclerosis (12–14), amyotrophic lateral sclerosis (15), spinal cord injury (16), and neuromyelitis optica (17). Current techniques for measuring T_1 in the spinal cord rely on the mere application of brain protocols to the cervical level of the spinal cord, mostly using the VFA method (18). However, the VFA method makes use of 3D (or 2D) spoiled gradient-echo acquisitions, which are inherently more sensitive to intrascan motion artifacts when compared with other approaches such as single-shot echo-planar imaging (EPI). If not properly addressed, these artifacts could propagate into the T_1 maps, especially in spinal cord applications, in which effects of physiological noise and subject motion are exacerbated. Additionally, several volumes (with varied flip angle) should be acquired to avoid noise bias in the fitting (19), complete magnetization spoiling has to be ensured (20), and an accurate map of the transmitted RF field (B_1) has to be obtained to correct for the actual flip angle at the voxel level (21). These facts contribute to preventing the design of fast, accurate, and robust protocols for T_1 mapping in the spinal cord using the VFA method.

In contrast, IR-based methods are less sensitive to the aforementioned limitations (9), and thus represent a more robust approach to for T_1 mapping in challenging environments such as the spinal cord, where multiple noise sources and field inhomogeneities coexist.

In this study, we introduce an IR-based T_1 mapping method for the spinal cord, making use of the slice-shuffling scheme initially developed for application to the brain (22,23). Our method allows for in vivo T_1 mapping of the whole cervical spinal cord in a clinically acceptable scan time. We demonstrate its intra- and intersubject reproducibility in a small cohort of healthy subjects.

METHODS

The slice-shuffling mechanism consists of cycling the order in which different slices are acquired over sequence repetitions. Here, we used the slice-shuffling mechanism in the context of T_1 mapping (22,23).

An IR sequence was developed for T_1 measurements in the spinal cord, making use of zonally oblique-magnified multislice (ZOOM) EPI (24–26), which allows artifact-free multislice imaging of small structures using a single-shot EPI readout. Slices are acquired with an interleaved order, allowing a time interval between contiguous slices excitation (TR) long enough for restoration of longitudinal magnetization after each oblique spin-echo pulse pair. This results in N_p groups (i.e., packages) of $N_{spp} = N_s/N_p$ maximally spaced-out slices acquired every TR, in which N_s is the total number of prescribed slices (Fig. 1a). An IR experiment is implemented using nonselective adiabatic inversion pulses, applied before the acquisition of each

package. Hyperbolic secant adiabatic inversion is used to achieve robust inversion over the target volume against B_1 and B_0 inhomogeneities (27).

Multiple inversion time (TI) data are acquired by shuffling the slice-acquisition order within the package for any of the M given delays between the inversion pulse and the first excited slice (TI_{app}) (i.e., for a given TI_{app}, a total of N_{spp} effective TIs are obtained). To avoid contamination between tilted slice excitations and inversion pulses, the TR is extended by a recovery time $T_{rec} = 6$ s (Fig. 1b).

The combination of IR preparation with a rapid ZOOM-EPI readout allows the exploitation of the slice-shuffling mechanism to reduce dead time when large slice coverage is required. For a given stack of N_s slices grouped in N_p packages, and M different TI_{app}, resulting in $N_{spp} \times M$ different effective TIs (TI_{eff}), the total protocol time T_{prot} is

$$T_{prot} = \sum_{i=1}^{M} N_{spp} N_p [TI_{app,i} + \Delta t_s (N_{spp} - 1) + T_{rec}] \quad [1]$$

where uniform temporal slice spacing Δt_s is assumed. The sampled TIs can be chosen by rearranging Δt_s, TI_{app}, and potentially M, according to the specific applications that dictate coverage $N_s = N_p \times N_{spp}$, and scan time available T_{prot}. Although a theoretical investigation of protocol optimization is beyond the scope of this article, Equation [1] shows how different settings of N_{spp}, N_p, and M for the same N_s can be used to reduce T_{prot}, therefore providing the basis to exploit the interplay among sequence parameters N_s, N_p, N_{spp}, and sampling scheme parameters M, TI_{app}, and Δt_s in optimization procedures.

Five healthy volunteers (age range 27–37, 4 males, 1 female) were enrolled in the study. Imaging was performed on a Philips Achieva 3T (Philips Healthcare, Best, the Netherlands) MRI system with a 16-channel neurovascular coil, using parallel transmission technology.

The whole cervical spinal cord (i.e., C1–C7) was imaged using the following MR parameters: field of view (FOV) $= 64 \times 48\,mm^2$, in-plane voxel size $= 1 \times 1\,mm^2$, EPI train length $= 63$, echo time (TE) $= 22$ ms, partial Fourier factor $= 0.6$, 24 slices, 5 mm thick. Magnetization recovery was sampled using the IR-ZOOM-EPI sequence described previously, at 12 TIs obtained by grouping slices in $N_p = 4$ packages and using $M = 2$ different TI_{app} of 100 and 1300 ms, and slice temporal spacing $\Delta t_s = 200$ ms, to produce the following $TI_{eff} = 100$, 300, 500, 700, 900, 1100, 1300, 1500, 1700, 1900, 2100, and 2300 ms. A "noise-only" scan obtained without RF and gradients was added to characterize noise standard deviation (σ) in the quantification. Total protocol duration was 7 min, 6 s. Validation of the protocol against a standard single slice IR in phantoms is shown in Supporting Figures S1 and S2 and Supporting Table S1.

A structural 3D gradient-echo (3D-GRE) scan (flip angle $= 7°$, TR $= 19$ ms) was acquired for image registration and region-of-interest (ROI) definition.

The protocol was repeated in a separate session for each subject to assess the reproducibility. Within-subject motion across time points was corrected slice-wise by means of 2D linear transformations with 3 degrees of freedom (28,29) using a model-based image registration approach (30).

Straightening of spinal cords was performed on IR-ZOOM-EPI and 3D-GRE data based on (31), enabling inherent coregistration among different modalities and facilitating registration of a spinal cord template to 3D-GRE volumes in subsequent analysis.

The following mono-exponential signal-recovery model

$$S(TI) = M_0\left(1 - 2e^{\frac{-TI}{T_1}}\right) \quad [2]$$

was fitted to magnitude data using maximum likelihood estimation assuming Rician distributed noise, to estimate the equilibrium magnetization M_0 and T_1. σ was obtained from the noise-only scan after smoothing image intensities with a moving average filter (3×3 kernel size) and correcting for noise floor bias (32) as follows:

$$\sigma = \eta\sqrt{\frac{2}{\pi}} \quad [3]$$

where η is the image intensity of the noise-only scan, after smoothing.

Spinal cord ROIs were defined automatically via registration of a spinal cord template (23,24) to each individual 3D-GRE scan, separately for each session. Template registration was performed using the spinal cord toolbox (25), and refined by supplying cord white matter (WM) and gray matter (GM) masks obtained using the method found in (33). Four different ROIs were selected: (i) GM obtained from segmentation, (ii) WM dorsal column obtained by merging the fasciculus cuneatus and fasciculus gracilis atlases from the template, (iii) WM left lateral column (LC_L), and (iv) WM right lateral column (LC_R) obtained by merging the respective spinothalamic, spinoreticular, rubrospinal, and lateral corticospinal tracts atlases from the template.

The mean T_1 and standard deviation were measured in each ROI, and in the whole cord, for both sessions. The intersession coefficient of variation (COV) was calculated for each ROI using

$$COV = \frac{1}{N}\sum_{i=1}^{N} \sqrt{2}\frac{|T_1^{i,1} - T_1^{i,2}|}{T_1^{i,1} + T_1^{i,2}} \quad [4]$$

where $T_1^{i,j}$ refers to the mean T_1 of subject i (with $i = 1,2,..,5$) for session j ($j = 1,2$) in a specific ROI.

Reproducibility of T_1 estimates at the regional level was assessed using Bland-Altman plots, linear regression, and correlation analysis.

The intraclass correlation coefficient (ICC1,2) was calculated for ROIs pooled among subjects using a two-way random effects model (34,35). The ICC measures the fraction of the total variability attributable to differences among subject-specific ROIs.

RESULTS

An example of the acquired IR data is shown in Figure 2 for different cervical levels.

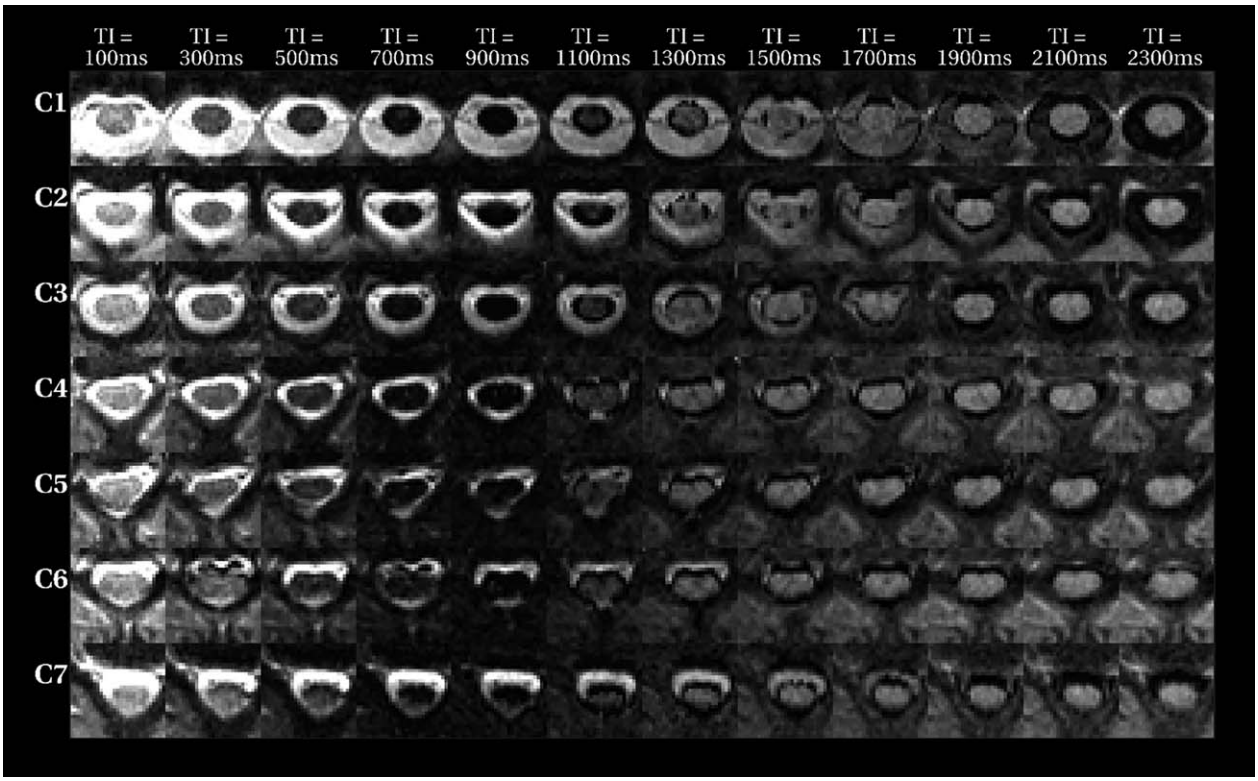

FIG. 2. Example of IR data acquired with ZOOM-EPI at varying TIs (from 100 to 2300 ms) in different cervical levels from a single subject.

T_1 maps at different vertebral levels of the cervical spinal cord (from C1 to C7) are shown in Figure 3 in a single subject. T_1 values appear very homogenous across all of the cord levels and show very little variability between scan and rescan maps.

Whole-cord T_1 mean, averaged across sessions and subjects, was 1142.3 (±148.2) ms. Regional T_1 values across subjects and sessions are given in Table 1. The average T_1 was 1108.5 (±77.2) ms for LC_L, 1110.1 (±83.2) ms for LC_R, 1150.4 (±102.6) ms for dorsal column, and 1136.4 (±90.8) ms for GM. Intersession COV for different ROIs was 0.93% for LC_L, 0.89% for LC_R, 0.74% for dorsal column, and 1.02% for GM. The COV for the whole-cord ROI was 0.95%.

Regional T_1 estimates showed good scan-rescan correlation, as demonstrated in Figure 3a. The Pearson correlation coefficient was 0.89 (P value < 0.01), and the slope of linear regression was 0.73 (confidence interval 0.54–0.92). The Bland-Altman plot in Figure 3b shows a negligible bias among T_1 estimates (2 ms), and very narrow 95% limits of agreement (approximatively ± 20 ms).

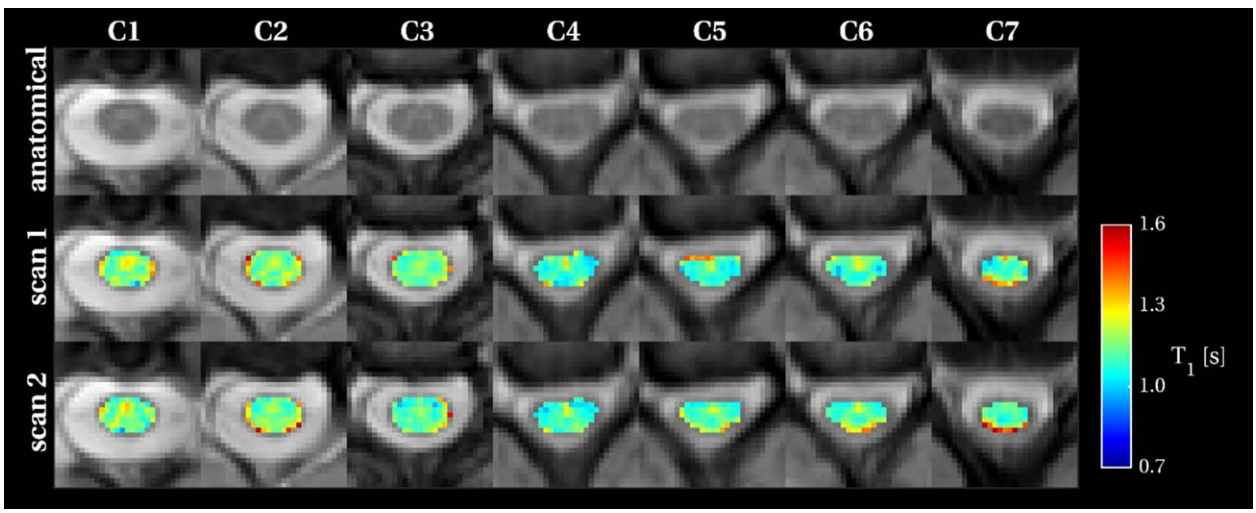

FIG. 3. Example of T_1 maps for scan and rescan in a single subject. An example slice is shown for each cervical level, together with the corresponding anatomical images in the top row.

Table 1
Mean and Standard Deviation for T_1 Estimates in Different ROIs and Whole Cord for Subjects, and Intersession COV for Each ROI Type.

		Region of Interest				
	Scan	LC_L	LC_R	Dorsal column	GM	Whole cord
Subject 1	1	1080.0 (61.3)	1088.7 (80.3)	1134.0 (61.6)	1103.3 (55.3)	1113.9 (80.4)
	2	1054.2 (103.0)	1074.1 (51.5)	1130.1 (118.3)	1098.8 (75.4)	1113.5 (129.7)
Subject 2	1	1097.3 (52.1)	1113.3 (85.0)	1134.4 (95.3)	1135.9 (57.2)	1135.9 (131.0)
	2	1097.5 (66.1)	1117.7 (75.7)	1138.7 (47.6)	1141.9 (64.9)	1129.8 (97.1)
Subject 3	1	1187.4 (89.8)	1151.6 (93.8)	1196.6 (97.2)	1188.0 (64.4)	1185.7 (105.8)
	2	1168.5 (99.1)	1155.3 (98.1)	1179.9 (74.1)	1166.6 (66.1)	1173.3 (132.7)
Subject 4	1	1113.9 (69.5)	1100.1 (70.6)	1183.5 (151.4)	1191.0 (246.9)	1187.3 (241.2)
	2	1120.1 (67.4)	1113.0 (77.8)	1181.8 (168.9)	1142.6 (119.1)	1168.0 (217.4)
Subject 5	1	1072.7 (81.0)	1077.0 (84.6)	1095.7 (124.4)	1099.3 (91.3)	1088.6 (137.1)
	2	1093.5 (82.7)	1110.6 (115.0)	1128.9 (87.0)	1096.3 (67.1)	1127.0 (210.3)
Mean (Std)		1108.5 (77.2)	1110.1 (83.2)	1150.4 (102.6)	1136.4 (90.8)	1142.3 (148.3)
COV		0.93%	0.89%	0.74%	1.02%	0.95%

Std, standard deviation.

The intraclass correlation coefficient for regional T_1 was 0.88 (P value < 0.01, confidence interval 0.71–0.95).

DISCUSSION AND CONCLUSIONS

In this study, we demonstrated a new, simple, fast, and reproducible method for mapping T_1 in the whole cervical spinal cord in vivo without deviating from the standard IR approach. Quantitative characterization of spinal cord microstructure is important in a variety of neurological disorders. More effort is required in developing robust methods to assess it, as many aspects of spinal cord microstructure are as yet uncharacterized in vivo with the current state of the art of quantitative MRI.

The proposed sequence, IR-ZOOM-EPI, combines advantageous solutions for T_1 mapping in the spinal cord. The use of a ZOOM-EPI readout to perform reduced FOV single-shot acquisition, which has previously been applied at 3 T in diffusion studies (36,37), while limiting distortions and freezing intrascan motion, is essential to achieve clinically feasible protocol durations. In fact, a previous in vivo T_1 mapping study in the spinal cord using IR required 20 min per slice and used a large FOV (18). In addition, the ZOOM-EPI readout is compatible with the magnetization preparation of an ideal IR experiment, in which inversion is performed by a nonspatially selective pulse. Because a TR constraint ($TR >> T_1$) is inherently in place with ZOOM-EPI to avoid cross-contamination from the oblique excitation pulse, the use of such an inversion pulse has a limited time penalty compared with the normal spin-echo sequence (the maximum TR increment is always lower than the maximum TI_{eff} chosen). The adiabatic inversion is also robust against magnetic field inhomogeneities, which are exacerbated in the spinal cord (11), and effects of the imperfect slice profile of the inversion pulse, thought to contribute to the variability of T_1 measurements (9).

Together with the adiabatic inversion, slice shuffling enables the optimal use of scan time (22,23,38), as a

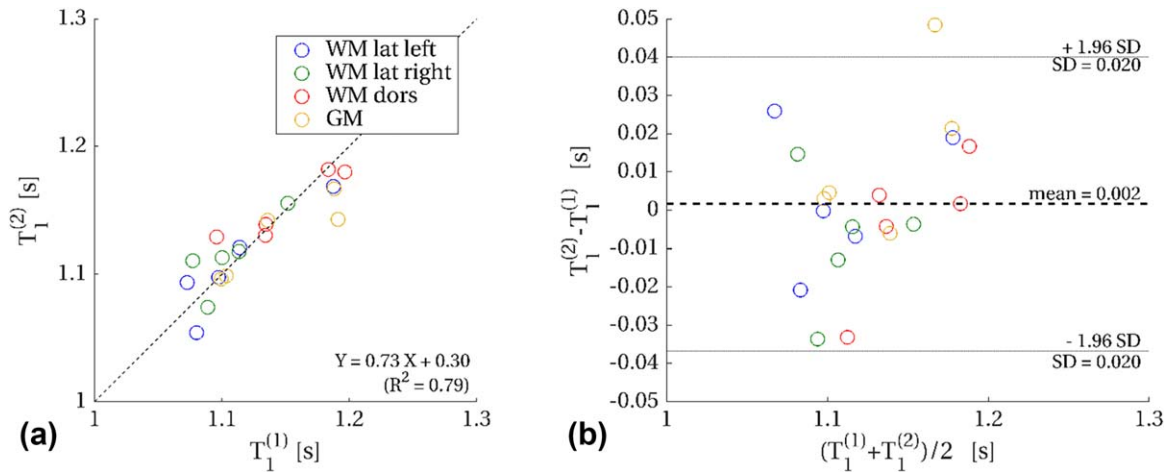

FIG. 4. **a**: Correlation between T_1 estimates from the first scan $T_1^{(1)}$ and second scan $T_1^{(2)}$. A total of 20 different mean T_1 values are obtained in a scan–rescan study from four different ROIs of five healthy subjects. Different ROI types are visualized with different colors: blue, left lateral column (LC_L); green, right lateral column (LC_R); red, dorsal column; yellow, GM. The dashed line shows the ideal identity between $T_1^{(1)}$ and $T_2^{(2)}$ mean estimates. Linear fit between mean T_1 estimates and coefficient of determination (R^2) are also reported. **b**: Bland–Altman plot for absolute agreement between T_1 estimates from first scan and second scan. Mean bias and 95% limits of agreement are shown with the dashed line and dotted lines, respectively.

range of effective TIs can be produced for the same nominal TR.

The combination of these factors into a single sequence allows the design of time-efficient T_1-mapping IR protocols for the spinal cord, of comparable duration to those using the VFA method with linear approximation fitting.

Quantitative T_1 values measured here lie within the expected range for tissues in the central nervous system at 3 T (39,40), with WM values being on the upper side of the reported values. This could be explained by the presence of larger WM axons (41), which leads to higher T_1 values for constant myelin volume fraction (3), or the presence of myelinated gray matter, as shown by histological findings (12,42). Other spinal cord studies, in which the T_1 was not the primary parameter of investigation, have indeed reported even higher values than those obtained here (43–45).

From the scan-rescan experiments we obtained excellent measures of reproducibility. Intersession COV was approximately 1% for all of the ROIs considered. This suggests that the T_1 can be measured precisely in the spinal cord using a relatively short protocol. Moreover, the high ICC values suggest that most of the variabilities in the T_1 estimates among subjects and ROIs derive from biological differences rather than measurement errors.

Limitations

Contrary to brain T_1 studies, we did not observe consistent contrast between WM and GM. As previously reported (18), this may be the result of the axial resolution used in this study ($1 \times 1\,mm^2$), which may not allow for clear delineation of the GM/WM boundaries, as well as contamination from cerebrospinal fluid flow. The use of higher resolution is warranted for pursuing detailed tissue specific analysis. Use of a 5-mm slice thickness is common in axial spinal cord imaging, and justified by the smooth variation of spinal cord anatomy in the cranial-caudal direction. However, the use of thinner slices could be beneficial for improving the accuracy of the tissue-specific characterization, as well as for the efficacy of motion correction techniques. Residual misalignments can in fact further confound the resultant WM/GM separation in parametric maps.

The periodic alternation of vertebrae and intervertebral disks along the spinal cord produces intensity signal variations in the slice direction (as seen along the columns of Fig. 2). The trend is evident also on maps displayed in Figure 3, with T_1 slightly decreasing with the cervical level, which is consistent with recent findings at ultra-high field (46). The implementation of techniques to mitigate signal intensity variation along the rostro–caudal direction, such as slice-wise z-shimming (47), should be considered in future studies to precisely assess the impact of this effect on T_1 estimation.

Future Improvements and Conclusions

The approach proposed here can be used in multimodal studies to better characterize spinal cord microstructure. IR-ZOOM-EPI has the potential to be extended to other spinal cord levels, as ZOOM-EPI has proven successful in diffusion studies at the lumbar level (48).

Additionally, more room for optimization is available in terms of parameter precision, via accurate selection of TIs with protocol optimization techniques (49,50) and acquisition time through combination with ultrafast imaging techniques (e.g., simultaneous multislice imaging (51)). The singular interplay among sequence parameters already allows scan time to be gained without needing to use acceleration techniques (i.e., N_{spp} and M can be arranged to provide a time-efficient protocol even when higher N_s are used). Formal optimization that accounts for protocol duration and TI selection could be devised starting with Equation [1], to produce an optimal T_1 protocol in the spinal cord, simultaneously addressing the issues of spatial coverage, SNR, protocol time, and T_1 estimate precision. Additional time gains could be used, in turn, to increase SNR through signal averaging for higher resolution imaging.

Alternative emerging approaches for T_1 mapping, such as MR fingerprinting (52), could allow further scan-time reduction, although its implementation to the spinal cord has not yet been proposed, and only applications to the brain are currently available.

In conclusion, reproducible measurements of T_1 can be obtained in the whole cervical spinal cord with a rapid protocol. Our method enables more comprehensive T_1 mapping studies in the spinal cord for different pathologies.

REFERENCES

1. Koenig S, Brown R, Spiller M, Lundbom N. Relaxometry of brain: why white matter appears bright in MRI. Magn Reson Med 1990;14: 482–495.
2. Gelman N, Ewing JR, Gorell JM, Spickler EM, Solomon EG. Interregional variation of longitudinal relaxation rates in human brain at 3.0 T: relation to estimated iron and water contents. Magn Reson Med 2001;45:71–79.
3. Harkins KD, Xu J, Dula AN, Li K, Valentine WM, Gochberg DF, Gore JC, Does MD. The microstructural correlates of t1 in white matter. Magn Reson Med 2016;75:1341–1345.
4. Vymazal J, Righini A, Brooks RA, Canesi M, Mariani C, Leonardi M, Pezzoli G. T1 and T2 in the brain of healthy subjects, patients with Parkinson disease, and patients with multiple system atrophy: relation to iron Content 1. Radiology 1999;211:489–495.
5. Henderson E, McKinnon G, Lee T-Y, and Rutt BK. A fast 3D Look-Locker method for volumetric T 1 mapping. Magn Reson Imaging 1999;17:1163–1171.
6. Freeman A, Gowland P, Mansfield P. Optimization of the ultrafast Look-Locker echo-planar imaging T1 mapping sequence. Magn Reson Imaging 1998;16:765–772.
7. Fram EK, Herfkens RJ, Johnson GA, Glover GH, Karis JP, Shimakawa A, Perkins TG, Pelc NJ. Rapid calculation of T1 using variable flip angle gradient refocused imaging. Magn Reson Imaging 1987;5:201–208.
8. Deoni SC, Rutt BK, Peters TM. Rapid combined T1 and T2 mapping using gradient recalled acquisition in the steady state. Mag Reson Med 2003;49:515–526.
9. Stikov N, Boudreau M, Levesque IR, Tardif CL, Barral JK, Pike GB. On the accuracy of T1 mapping: searching for common ground. Mag Reson Med 2015;73:514–522.
10. Wheeler-Kingshott C, Stroman PW, Schwab J, et al. The current state-of-the-art of spinal cord imaging: applications. NeuroImage 2014;84: 1082–1093.
11. Stroman PW, Wheeler-Kingshott C, Bacon M, et al. The current state-of-the-art of spinal cord imaging: methods. NeuroImage 2014;84: 1070–1081.

12. Gilmore CP, DeLuca GC, Bö L, Owens T, Lowe J, Esiri MM, Evangelou N. Spinal cord neuronal pathology in multiple sclerosis. Brain Pathol 2009;19:642–649.
13. Gilmore CP, Bö L, Owens T, Lowe J, Esiri MM, Evangelou N. Spinal cord gray matter demyelination in multiple sclerosis—a novel pattern of residual plaque morphology. Brain Pathol 2006;16:202–208.
14. C. Gilmore, J. Geurts, N. Evangelou, J. Bot, R. Van Schijndel, P. Pouwels, et al. Spinal cord grey matter lesions in multiple sclerosis detected by post-mortem high field MR imaging. Multiple Sclerosis J 2009;15:180–188.
15. Bede P, Bokde AL, Byrne S, Elamin M, Fagan AJ, Hardiman O. Spinal cord markers in ALS: diagnostic and biomarker considerations. Amyotrophic Lateral Sclerosis 2012;13:407–415.
16. Dietz V, Curt A. Neurological aspects of spinal-cord repair: promises and challenges. Lancet Neurol 2006;5:688–694.
17. Wingerchuk DM, Lennon VA, Lucchinetti CF, Pittock SJ, Weinshenker BG. The spectrum of neuromyelitis optica. Lancet Neurol 2007;6:805–815.
18. Smith SA, Edden RA, Farrell JA, Barker PB, Van Zijl P. Measurement of T1 and T2 in the cervical spinal cord at 3 tesla. Magn Reson Med 2008;60:213–219.
19. Chang LC, Koay CG, Basser PJ, Pierpaoli C. Linear least-squares method for unbiased estimation of T1 from SPGR signals. Magn Reson Med 2008;60:496–501.
20. Yarnykh VL. Optimal radiofrequency and gradient spoiling for improved accuracy of T1 and B1 measurements using fast steady-state techniques. Magn Reson Med 2010;63:1610–1626.
21. Lee Y, Callaghan MF, Nagy Z. Analysis of the precision of variable flip angle T1 mapping with emphasis on the noise propagated from RF transmit field maps. Front Neurosci 2017;11:106.
22. Ordidge R, Gibbs P, Chapman B, Stehling M, Mansfield P. High-speed multislice T1 mapping using inversion-recovery echo-planar imaging. Magn Reson Med 1990;16:238–245.
23. Clare S, Jezzard P. Rapid T1 mapping using multislice echo planar imaging. Magn Reson Med 2001;45:630–634.
24. Symms M, Wheeler-Kingshott C, Parker G, Barker G. Zonally-magnified oblique multislice (ZOOM) EPI. In Proceedings of the 8th annual meeting of the ISMRM, Denver, Colorado, USA, 2000.
25. Wheeler-Kingshott CA[1], Hickman SJ, Parker GJ, Ciccarelli O, Symms MR, Miller DH, Barker GJ. Investigating cervical spinal cord structure using axial diffusion tensor imaging. NeuroImage 2002;16:93–102.
26. Wheeler-Kingshott CA, Parker GJ, Symms MR, Hickman SJ, Tofts PS, Miller DH, Barker GJ. ADC mapping of the human optic nerve: increased resolution, coverage, and reliability with CSF-suppressed ZOOM-EPI. Magn Reson Med 2002;47:24–31.
27. Norris DG. Adiabatic radiofrequency pulse forms in biomedical nuclear magnetic resonance. Concept Magn Reson 2002;14:89–101.
28. Jenkinson M, Bannister P, Brady M, Smith S. Improved optimization for the robust and accurate linear registration and motion correction of brain images. NeuroImage 2002;17:825–841.
29. Jenkinson M, Smith S. A global optimisation method for robust affine registration of brain images. Med Image Anal 2001;5:143–156.
30. Ben-Amitay S, Jones DK, Assaf Y. Motion correction and registration of high b-value diffusion weighted images. Magn Reson Med 2012;67: 1694–1702.
31. Leener B, Mangeat G, Dupont S, Martin AR, Callot V, Stikov N, Fehlings MG, Cohen-Adad J. Topologically preserving straightening of spinal cord MRI. J Magn Reson Imaging 2017. doi: 10.1002/jmri.25622.
32. Jones DK, Basser PJ. 'Squashing peanuts and smashing pumpkins': How noise distorts diffusion-weighted MR data. Magn Reson Med 2004;52:979–993.
33. Prados F, Cardoso MJ, Yiannakas MC, et al. Fully automated grey and white matter spinal cord segmentation. Sci Rep 2016;6.
34. McGraw KO, Wong SP. Forming inferences about some intraclass correlation coefficients. Psychol Methods 1996;1:30.
35. Shrout PE, Fleiss JL. Intraclass correlations: uses in assessing rater reliability. Psychol Bull 1979;86:420.
36. Grussu F, Schneider T, Zhang H, Alexander DC, Wheeler–Kingshott CA. Neurite orientation dispersion and density imaging of the healthy cervical spinal cord in vivo. NeuroImage 2015;111:590–601.
37. Samson RS, Lévy S, Schneider T, Smith AK, Smith SA, Cohen-Adad J, Wheeler-Kingshott CA. ZOOM or non-ZOOM?. Assessing spinal cord diffusion tensor imaging protocols for multi-centre studies. PloS One 2016;11:e0155557.
38. Zhu DC, Penn RD. Full-brain T1 mapping through inversion recovery fast spin echo imaging with time-efficient slice ordering. Magn Reson Med 2005;54:725–731.
39. Stanisz GJ, Odrobina EE, Pun J, Escaravage M, Graham SJ, Bronskill MJ, Henkelman RM. T1, T2 relaxation and magnetization transfer in tissue at 3T. Magn Reson Med 2005;54:507–512.
40. Lu H, Nagae-Poetscher LM, Golay X, Lin D, Pomper M, van Zijl P. Routine clinical brain MRI sequences for use at 3.0 Tesla. J Magn Reson Imaging 2005;22:13–22.
41. Makino M, Mimatsu K, Saito H, Konishi N, Hashizume Y. Morphometric study of myelinated fibers in human cervical spinal cord white matter. Spine 1996;21:1010–1016.
42. Grussu F, Schneider T, Yates RL, Tachrount M, Newcombe J, Zhang H, Alexander DC. Histological metrics confirm microstructural characteristics of NODDI indices in multiple sclerosis spinal cord. In Proceedings of the 23rd Annual Meeting of the ISMRM, Toronto, Ontario, Canada, 2015. p 909.
43. Duval T, Lévy S, Stikov N, et al. g-Ratio weighted imaging of the human spinal cord in vivo. NeuroImage 2017;145:11–23.
44. Smith AK, Dortch RD, Dethrage LM, Smith SA. Rapid, high-resolution quantitative magnetization transfer MRI of the human spinal cord. NeuroImage 2014;95:106–116.
45. Samson R, Ciccarelli O, Kachramanoglou C, Brightman L, Lutti A, Thomas DL, Weiskopf N, Gandini Wheeler-Kingshott CA. Tissue-and column-specific measurements from multi-parameter mapping of the human cervical spinal cord at 3 T. NMR Biomed 2013;26:1823–1830.
46. Massire A, Taso M, Besson P, Guye M, Ranjeva J-P, Callot V. High-resolution multi-parametric quantitative magnetic resonance imaging of the human cervical spinal cord at 7T. NeuroImage 2016;143:58–69.
47. Finsterbusch J, Eippert F, Büchel C. Single, slice-specific z-shim gradient pulses improve T2*-weighted imaging of the spinal cord. NeuroImage 2012;59:2307–2315.
48. Yiannakas MC, Grussu F, Louka P, Prados F, Samson RS, Battiston M, Altmann DR, Ourselin S, Miller DH, Gandini Wheeler-Kingshott CA. Reduced field-of-view diffusion-weighted imaging of the lumbosacral enlargement: a pilot in vivo study of the healthy spinal cord at 3T. PLoS One 2016;11:e0164890.
49. Becker ED, Ferretti JA, Gupta RK, Weiss GH. The choice of optimal parameters for measurement of spin-lattice relaxation times. II, Comparison of saturation recovery, inversion recovery, and fast inversion recovery experiments. J Magn Reson (1969) 1980;37:381–394.
50. Ogg RJ, Kingsley PB. Optimized precision of inversion-recovery T1 measurements for constrained scan time. Magn Reson Med 2004;51: 625–630.
51. Setsompop K, Gagoski BA, Polimeni JR, Witzel T, Wedeen VJ, Wald LL. Blipped-controlled aliasing in parallel imaging for simultaneous multislice echo planar imaging with reduced g-factor penalty. Magn Reson Med 2012;67:1210–1224.
52. Ma D, Gulani V, Seiberlich N, Liu K, Sunshine JL, Duerk JL, Griswold MA. Magnetic resonance fingerprinting. Nature 2013;495: 187–192.

SUPPORTING INFORMATION

Additional Supporting Information may be found in the online version of this article.

Fig. S1. Comparison of T_1 estimates in phantoms between standard IR (**a**) and IR-ZOOM-EPI (**b**). The IR-ZOOM-EPI is repeated separately on each phantom (with the respective FOV highlighted in the corner of each map). $N_s = 6$ slices were acquired. The central slice is shown here for the purpose of comparison.

Fig. S2. Correlation plots between T_1 estimates from standard IR and IR-ZOOM-EPI with $T_{rec} = 10$ s (**a**), $T_{rec} = 8$ s (**b**), and $T_{rec} = 6$ s (**c**). In each plot, the widths of the marker in each direction (horizontal and vertical) correspond to the width of the relative distribution (standard IR and IR-ZOOM-EPI) within the 1st and 99th percentile. The identity line (indicating an ideal linear relationship), together with parameters for the linear fit of T_1 from IR-ZOOM-EPI against T_1 from IR single slice, are shown. The bar graph (**d**) shows a quantitative comparison between T_1 estimates in all of the phantoms. The bar height represents the mean T_1 value, whereas the error bars indicate the 99th percentile of the distribution. No differences between standard IR and all versions of IR-ZOOM-EPI were detected by a paired t-test.

Table S1. Mean and Standard Deviation of T_1 Estimates in the Phantoms for Standard IR Single Slice, IR-ZOOM-EPI With $T_{rec} = 10$ s, IR-ZOOM-EPI With $T_{rec} = 8$ s, and IR-ZOOM-EPI With $T_{rec} = 6$ s